

Terminal Impedance and Antenna Current Distribution of a VLF Electric Dipole in the Inner Magnetosphere

Timothy W. Chevalier, Umran S. Inan, *Fellow, IEEE*, and Timothy F. Bell

Abstract—The current distribution and input impedance of an electric dipole antenna operating in a cold magnetoplasma at very low frequency (VLF) is determined through numerical simulation. A full wave solution of Maxwell's equations using a finite-difference frequency-domain (FDFD) method is implemented to simulate electromagnetic wave propagation in this highly anisotropic medium. The classical perfectly matched-layer (PML) boundary condition is found to exhibit instabilities in the form of nonphysical wave amplification in this environment. To circumvent these difficulties, a PML is developed that is tailored to the cold plasma environment at VLF frequencies. It is shown that the current distribution for antennas with length < 100 m is approximately triangular for magnetospheric conditions found at $L = 2$ and $L = 3$ in the geomagnetic equatorial plane. Calculated variations of input impedance as a function of drive frequency are presented for two case studies and compared with predictions of existing analytical work.

Index Terms—Antenna, plasma.

I. INTRODUCTION

ELECTRIC dipole antennas are commonly used in space plasmas with applications that range from radio frequency probing of the magnetosphere to plasma diagnostics [1]–[4]. The radiation pattern and efficiency of an antenna is directly related to the distribution of currents flowing along its surface. For electrically short dipole antennas operating in a free-space environment, the current distribution is known to be triangular [5, pp. 40–42]. For an antenna operating in a magnetoplasma however, the situation is more complex with single-frequency wavelengths that vary by several orders of magnitude as a result of the high anisotropy of the medium.

The coupling of antennas with a magnetized plasma has been an area of active research for decades. The work of [6] performed some of the first analytical studies concerning the behavior of electric dipole antennas in a cold magnetoplasma. Formulas for the input impedance of short cylindrical dipoles of arbitrary orientation with respect to the background magnetic field using quasi-electrostatic theory were derived assuming a

lossy (i.e., collisional) plasma. The analysis was limited to electrically short antennas (relative to a free-space wavelength) so that a triangular current distribution along the length of the antenna was assumed to be valid. In addition, Balmain [6] compares his theoretical results with experiment for combinations of neon and argon plasmas obtaining good agreement. Subsequently, Balmain in [7] and [8] provides nice reviews of the relevant literature to date involving the status of antenna research for a variety of plasma environments and antenna types including dipole and loop antennas. These review papers cover such topics as impedance, radiation, resonances, and nonlinearities for both isotropic and anisotropic plasmas. Unfortunately, very little research up until the review paper by [8] included antennas operating in a collisionless magnetoplasma at very low frequency (VLF) with the dominant research on the subject having been performed by [9]–[14].

In [9], closed-form analytical expressions for the radiation resistance of electric dipole antennas operating in a cold magnetoplasma were developed using a full wave approach. The frequency range considered included whistler-mode frequencies (i.e., below the electron gyrofrequency) well above the lower hybrid resonance (LHR) frequency denoted as f_{LHR} . Antenna orientations both parallel and perpendicular to the background magnetic field were considered in this work assuming an electron–proton plasma. In addition to the work of [9], Wang and Bell in [10] extend their previous analysis to include the frequency range below f_{LHR} and calculate the radiation resistance for electric-dipole antennas of arbitrary orientation with respect to the background magnetic field. In addition to highlighting the fact that although Balmain's electrostatic approximation in [6] is valid for frequencies well above f_{LHR} , the authors of [10] point out that this same electrostatic theory predicts a purely imaginary radiation resistance below f_{LHR} . Furthermore, they conclude that more power will be radiated from a dipole antenna oriented perpendicular to the background magnetic field since the propagating modes launched from this orientation provide a much higher radiation resistance with efficiencies greatly exceeding those found for the same antenna in free space and provide a frequency range for which their full wave theory is valid for a 100-m antenna; this range being $f < 1.4f_{LHR}$ and $f < 1.16f_{LHR}$ for magnetospheric locations corresponding to $L = 2$ and $L = 3$, respectively, where the parameter L represents the radial distance in units of one Earth radius, from the center of the Earth to the position of the magnetic field line at the magnetic equatorial plane. In the same year, [11] provides formulas for the input impedance of VLF antennas operating in a magnetoplasma.

Manuscript received April 27, 2006; revised January 26, 2008. Published August 6, 2008 (projected). This research was supported by the AFOSR under Grant F49620-03-1-0338 and by the High-Frequency Active Auroral Research Program (HAARP).

The authors are with the Space, Telecommunications, and Radioscience Laboratory, Department of Electrical Engineering, Stanford University, Stanford, CA 94305 USA (e-mail: timothychevalier@stanford.edu; inan@nova.stanford.edu; bell@nova.stanford.edu).

Digital Object Identifier 10.1109/TAP.2008.927497

In following work, formulas for the radiation patterns of arbitrarily oriented electric and magnetic dipoles in a cold collisionless magnetoplasma were derived [12]. Expressions for the power patterns were given for various values of driving frequency and magnetospheric location. The authors of [12] conclude in this work that the refractive index surface that governs wavelength and propagation direction dominates the focusing of the radiation which changes from the resonance cone direction (propagation direction in a cold magnetized plasma for which the refractive index approaches infinity), for frequencies that are a factor of 0.75 the electron gyrofrequency to a pencil beam pattern focused along the static magnetic field for lower frequencies that lie within the whistler-mode regime. In [13], Wang and Bell examine the radiation characteristics of an electric dipole at VLF frequencies in a warm magnetoplasma by adding a finite electron temperature effect incorporated through the addition of a scalar pressure term in the cold plasma equations, a commonly used practice at this time [8]. They assert that for frequencies above f_{LHR} , propagation characteristics may be significantly altered since the thermally modified whistler mode can propagate at angles beyond the resonance cone, however, for frequencies below f_{LHR} , the refractive index surface is basically unmodified while noting radiation efficiencies for the perpendicular antenna greater than at least 10% over the parallel antenna for most cases. In addition, the authors of [13] omit the nonlinear sheath (region of nonneutrality that is quasi-electrostatic in nature surrounding a conductor immersed in a plasma [15]) problem assuming low-voltage antenna operation and use a Fourier decomposition of the wave and plasma equations of motion to solve the system of equations. During the same period, studies of whistler-mode radiation patterns of electric dipole antennas in a laboratory setting were performed [16] providing some reassurance to the findings in [12]. Even with all of these advancements, the primary underlying assumption made in [9]–[14] was that the current distribution along the length of the antenna was assumed to be triangular for the formulas derived in these works. Some of the more recent analytical work performed on the subject is that of [17]. In this paper, the input impedance of short dipole antennas operating at high frequencies (HF) in an ionospheric plasma was compared assuming both triangular and exponential current distributions along the length of the antenna. As in [6], Nikitin and Swenson [17] used a quasi-electrostatic approach to determine the terminal properties for an antenna with orientation parallel to the static magnetic field. The impedance values in [17] demonstrate good agreement with the results of [6] for frequencies between the electron gyrofrequency and upper hybrid frequency inclusive but for highly collisional ionospheric conditions found at a 100-km altitude, which are not applicable to studies at VLF in a collisionless magnetospheric environment.

Simulation work involving antennas operating in a magnetized plasma environment is scarce with [18] constituting some of the first modeling attempts on the subject. The authors of [18], utilizing a warm plasma model, determined the terminal impedance of very short dipole antennas in a collisional ionospheric plasma in the absence of an effective boundary condition using the finite-difference time-domain (FDTD) method. Their model assumes an incompressible Maxwellian fluid for the electrons using the first two moments of the Boltzmann equation for electrons only while the ions and neutrals remain stationary. As

in [13], a scalar pressure is assumed for the electrons. Current distributions and impedance values are determined for a 1-m linear antenna with results compared once again to Balmain's electrostatic model [6] with good agreement. The authors circumvent undetermined boundary condition instabilities by terminating the simulations before reflections from the boundary can contaminate the solution results.

The topic of antenna–plasma interactions has received recent attention with the renewed interest in the study of various mechanisms for the precipitation (removal) of energetic electrons from the Earth's radiation belts [19]. The work of [19] concludes that *in situ* injection of VLF whistler-mode waves can reduce the lifetime of 1500-keV electrons by a factor of two, thereby reducing the radiation damage to satellites that orbit within this region of space. The primary motivation for this work is to quantify the requirements for controlled precipitation of radiation belt particles using space-based VLF transmitters. The coupling of the antenna to its environment is of primary importance in this context with coupling occurring in a number of distinct regions. Close to the antenna exists a plasma sheath, which directly affects the terminal impedance properties (and hence tuning parameters) of the antenna. Inside the sheath region, electrostatic effects are dominant and particle energization may be significant for large applied voltages. Beyond this region, the electromagnetic waves are of a low enough intensity such that the environment can be well described by a cold plasma treatment.

To optimally inject VLF waves and thereby maximize energetic electron precipitation, it is necessary to determine the radiation pattern of the antenna. Though the antenna tuning properties are dominated by the nonlinear electrostatic sheath in the immediate vicinity of the antenna, the far-field pattern is determined by the current distribution along the antenna. As closure relations for the infinite set of fluid moments continue to be pursued and particle-in-cell (PIC) codes remain intractable for near- and far-field antenna simulations of collisionless magnetoplasmas [20], our goal is not to provide detailed analysis of nonlinear sheath dynamics or wave–particle interactions but to provide methods for treating the difficulties inherent in model formulations involving the solution of Maxwell's equations in a collisionless magnetized plasma environment within the VLF range. In this paper, we determine the current distribution and terminal impedance properties of a dipole antenna in the absence of a sheath using a cold plasma treatment. As such, our results can be viewed as being particularly applicable to the cases in which the drive voltages applied on the antenna are relatively small compared to the background plasma potential given by the relation $q\Phi = (3/2) kT$ where q is the charge of an electron, Φ is the potential, and the quantity $(3/2) kT$ represents the thermal energy of the particles. In this context, our results constitute an extension of the work of [9]–[11], who also considered the problem in the absence of a sheath and analytically determined the terminal impedance parameters under the assumption of a triangular current distribution. For large applied voltages, however, the nonlinear sheath dynamics would need to be addressed and is beyond the scope of this paper.

Unlike the work of [9]–[11], however, we make no assumptions about the form of the current distribution. Instead, the current distribution and the terminal properties of the antenna are determined through simulation in a fully self-consistent manner.

Because past analytical formulations are only valid for simple dipole geometries in a linear environment, we use numerical methods that are not subject to these constraints. Our numerical approach allows for a relatively straightforward extension into regimes for which there are no analytical solutions such as inhomogeneous plasmas or more complex antenna designs.

FDFD is the frequency-domain counterpart of the well-established FDTD technique [21]. Though literature on the application of FDFD to wave propagation in a magnetoplasma is scarce, there have been several applications of the FDTD method to the subject of wave propagation through a plasma, which are directly applicable to simulation using the FDFD method.

The flexibility and generality of the FDTD method accounts for its acceptance as the method of choice for electromagnetic wave interaction within complex media [21]. Such media includes plasmas, and more recently, metamaterials with [22] providing an analysis of anisotropic magnetic materials for antenna applications in the very high frequency (VHF) and ultrahigh frequency (UHF) bands. As it pertains to the study of plasmas, Cummer [23] provides a detailed comparison of the methods used to date; however, the works mentioned deal strictly with isotropic plasmas. The authors of [24] address the problem of electromagnetic wave propagation inside a cold magnetoplasma using FDTD but do not address the application of absorbing boundary conditions (ABCs) for the reflectionless absorption of outgoing waves. In this paper, we show that ABCs are one of the most difficult and pervasive issues underlying the simulation of electromagnetic wave propagation in a magnetoplasma.

Since the introduction of the perfectly matched layer (PML) [25], it has been used extensively in the field of computational electromagnetics due to its superiority over other types of ABCs. The PML, however, suffers from instabilities in the presence of some anisotropic media such as orthotropic materials as discussed in [26]. As demonstrated in [26], this instability is not unique to a particular system of equations; rather, it is inherent in all PML derivations since they share the same underlying structure. In this paper, we show that this numerical instability is present within the context of magnetized plasma simulations that need to be used to solve Maxwell's equations with a PML boundary condition. Also, this instability is independent of the method used for the plasma dynamics or the type of time integration scheme used. Thus, PIC, fluid, time, and frequency-domain methods are all affected by the presence of this numerical instability.

The purpose of this paper is to demonstrate the complexity involved in numerically modeling the near-field properties of electric dipole antennas operating in a cold, collisionless, magnetized plasma specifically emphasizing some of the numerical challenges in connection with PML boundary conditions and wave propagation in such media. We present comparisons of the results of our simulations with available analytical results for both the current distribution and input impedance to provide confidence in our methods as well as affirm assumptions made in past analytical work.

II. THEORETICAL FORMULATION

The cold plasma description we use for our FDFD modeling combines the first two linearized moments of Vlasov's equation

with Maxwell's equations. The final system of equations representing our cold plasma model is given by:

$$\nabla \times \vec{H} = \sum_N \vec{J}_\alpha + \epsilon_o \frac{d\vec{E}}{dt} \quad (1a)$$

$$\nabla \times \vec{E} = -\mu_o \frac{d\vec{H}}{dt} \quad (1b)$$

$$\frac{d\vec{J}_\alpha}{dt} + \nu_\alpha \vec{J}_\alpha = \frac{q_\alpha}{m_\alpha} \left(q_\alpha n_\alpha \vec{E} + \vec{J}_\alpha \times \vec{B}_o \right) \quad (1c)$$

where \vec{E} and \vec{H} are the wave *electric* and *magnetic* fields, and J , ν , n , q , and m are the *current density*, *collision frequency*, *number density*, *charge*, and *mass* of species α . Equation (1c) represents a simplified version of the generalized Ohm's law.

For the purpose of this work, the dipole antennas are taken to be located between $L = 2$ and $L = 3$ near the magnetic equatorial plane corresponding to distances of approximately two and three Earth radii from the center of the earth. The plasma in this region is fully ionized and is composed of hydrogen ions and electrons. At $L = 2$, the plasma and gyrofrequencies are taken to be $f_{pe} = 401$ kHz and $f_{ce} = 110$ kHz, respectively [1]. Because the densities of neutrals and electrons at this location are low, we assume a collisionless environment.

III. SIMULATION PROPERTIES

A. Computational Mesh Setup

The numerical mesh used for the cold electromagnetic plasma simulation is based on the traditional staggered/interleaved FDTD mesh for locations of electric and magnetic fields [27]. The currents described by (1c) are spatially colocated with their electric field counterpart. Care must be taken in the placement of the components of the current \vec{J} . Recent papers on the subject such as [24] propose collocating all components of the currents at the corner of the electric field Yee cell. Unfortunately, such positioning of the currents produces spurious electrostatic waves, which possess a spatial wavelength on the order of the mesh cell size. Such numerical waves are a result of the spatial averaging of the currents and are explained as follows.

Referring to Fig. 1, which represents the computational grid of [24], the locations of the electric fields are 1/2 a cell width away from the corresponding components of the current density \vec{J} described by (1c). Spatial averaging of a field value is necessary when the field quantity at a given location on the computational mesh is desired but not available. For instance, the update equation for the electric field described by (1a) requires values of the current density \vec{J} . Because the components of \vec{J} are not colocated with the corresponding components of electric field on the mesh, a suitable average must be made, i.e., averaging \vec{J}_x at the location of \vec{E}_x . The same type of process holds true for the current density update equations presented by (1c). Removing all references to time, the grid of [24] requires the averaging given by (2a)–(2c) to spatially colocate the electric field components of \vec{E} with the corresponding component of the current density \vec{J} given by (1c)

$$E_x \Big|_{J_x} = \frac{1}{2} \left(E_x \Big|_{i+(1/2),j,k} + E_x \Big|_{i-(1/2),j,k} \right) \quad (2a)$$

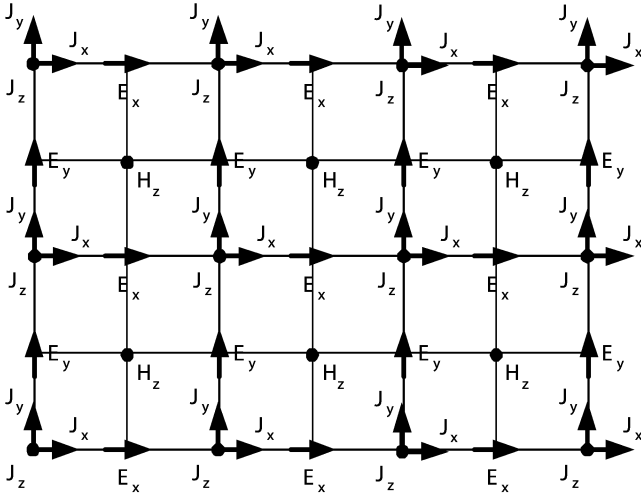


Fig. 1. Two-dimensional grid of Lee and Kalluri.

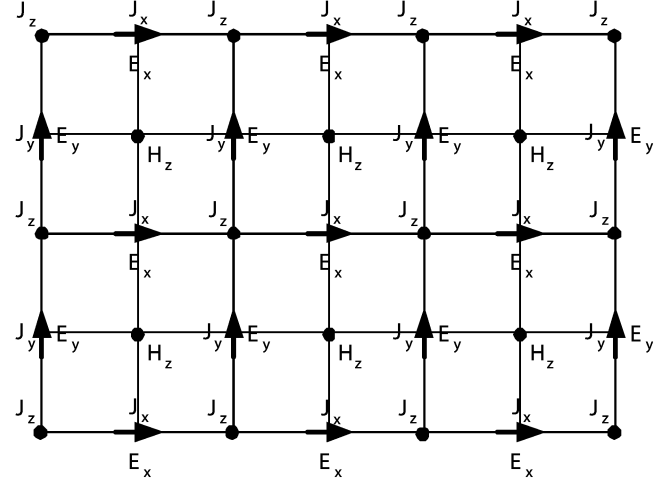


Fig. 3. Two-dimensional grid used in present model.

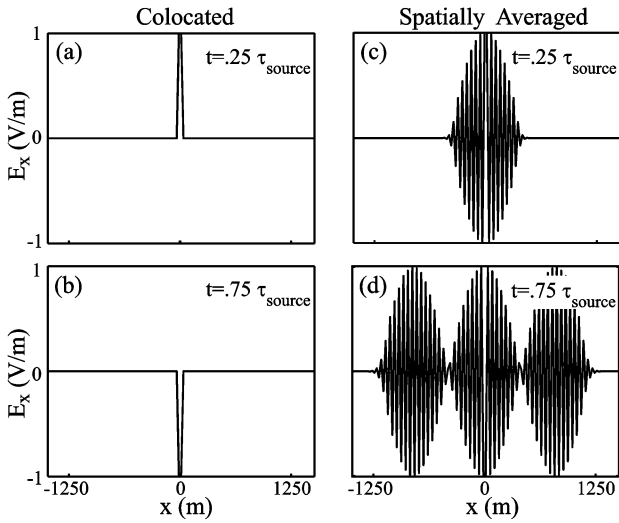


Fig. 2. One-dimensional time-domain simulation in cold plasma depicting nonphysical electrostatic wave formation on spatially averaged mesh versus collocated mesh taken at times $t = (\tau/4)$ and $t = (3\tau/4)$ where τ represents the period of a 20-kHz sine wave. (a) Collocated E-field at time $t = 0.25\tau$. (b) Collocated E-field at time $t = 0.75\tau$. (c) Spatially averaged E-field at time $t = 0.25\tau$. (d) Spatially averaged E-field at time $t = 0.75\tau$.

$$E_y|_{J_y} = \frac{1}{2} \left(E_y|_{i,j+(1/2),k} + E_y|_{i,j-(1/2),k} \right) \quad (2b)$$

$$E_z|_{J_z} = \frac{1}{2} \left(E_z|_{i,j,k+(1/2)} + E_z|_{i,j,k-(1/2)} \right) \quad (2c)$$

For frequencies f , $f_{LHR} < f < f_{ce}$, propagation in directions orthogonal to the static magnetic field is not supported in a cold plasma. This fact is verified with reference to Figs. 7 and 8, as further discussed in Section III-F. Using a Cartesian coordinate system and assuming a $+\hat{z}$ directed static magnetic field, any electric field components excited in the $+\hat{x}$ or $+\hat{y}$ direction subsequently produce currents in that respective direction through the spatial averaging of (2a). The recursive process of spatial averaging leads to nonphysical electrostatic waves (of numerical origin), which propagate in a direction orthogonal to the static magnetic field as shown in Fig. 2.

The formation of these nonphysical wave modes is most easily demonstrated in the time domain. As such, Fig. 2 represents a 1-D time-domain simulation showing the formation of nonphysical electrostatic waves resulting from the spatial averaging of (2a). A 20-kHz sinusoidal \vec{E}_x source is placed in the center of the space in Fig. 2. The medium is a cold plasma with properties consistent with those found at $L = 2$. The horizontal axis represents the \hat{x} dimension, with a static magnetic field present in the $+\hat{z}$ direction. Because there are neither propagating nor evanescent wave modes supported in this scenario, we would expect to see only the source point oscillating in a sinusoidal fashion. Fig. 2(a) and (b) represents simulation snapshots at $t = (\tau/4)$ and $t = (3\tau/4)$, respectively, for a mesh in which \vec{E}_x is collocated with \vec{J}_x . Fig. 2(c) and (d) represents a mesh in which \vec{E}_x and \vec{J}_x are staggered in space per (2a). It is seen that the collocation of \vec{E}_x and \vec{J}_x found in Fig. 2(a) and (b) correctly captures the physics (with only the source point oscillating in time) while the staggered mesh of Fig. 2(c) and (d) produces an electrostatic wave (possessing no associated magnetic field) that propagates along the \hat{x} direction. In fact, the only frequency range that supports electrostatic wave propagation in a cold plasma environment is that associated with the extraordinary mode. This mode that is discussed in Section III-F in conjunction with Z-mode propagation is denoted by “X” in Fig. 5, which resides above the plasma frequency; a frequency well above the 20-kHz source, being 401 kHz at $L = 2$ in the equatorial plane. Thus, the oscillations seen in Fig. 2(c) and (d) must be nonphysical in nature.

To prevent the formation of these nonphysical waves, the components of current density \vec{J} for each species are collocated with their electric field counterpart as shown in Fig. 3 and applied to our FDFD formulation. Although our model utilizes spatial averaging, the averaging does not appear to create nonphysical modes.

B. Frequency-Domain Technique

The use of frequency-domain techniques over those based on time integration (FDTD, for instance) allows for the accurate modeling of spatial structures that are orders of magnitude smaller than a wavelength without an appreciable increase in

computation time. This feature is a major advantage in our case, considering that the wavelengths for VLF waves below the electron gyrofrequency considered in this paper range from meters to megameters in the same simulation due to the high anisotropy of the refractive index. Refractive index surfaces will be discussed later in Sections III-E and III-F.

Our model uses the portable expression template for scientific computing (PETSc) framework [28], [29] for both its embedded parallelism and integrated linear and nonlinear solvers, which are integral parts of the frequency-domain methods used. The FDFD technique solves for the sinusoidal steady-state response of a single-frequency excitation. To solve our system of (1a)–(1c), we must transform them into the frequency domain making the following substitution for the time derivative operator: $(d/dt) = j\omega$. This results in

$$\nabla \times \vec{H} = \sum_N \sigma_\alpha \vec{E} + \epsilon_o j\omega \vec{E} \quad (3a)$$

$$\begin{aligned} \nabla \times \vec{E} &= -\mu_o j\omega \vec{H} \\ \sigma_\alpha &= \epsilon_o \omega_p^2 (j\omega I - \Omega)^{-1} \\ \Omega &= \begin{pmatrix} -\nu & -\omega_{bz} & \omega_{by} \\ \omega_{bz} & -\nu & -\omega_{bx} \\ -\omega_{by} & \omega_{bx} & -\nu \end{pmatrix} \end{aligned} \quad (3b)$$

where σ_α represents the conductivity matrix in the relation $J = \sigma \vec{E}$ resulting from the transformation of (1c) into the frequency domain. I represents the identity matrix and $\omega_b = (|q|B_o/m_e)$ is the electron gyrofrequency where B_o represents the magnitude of the static magnetic field.

Frequency-domain methods require a large complex matrix inversion. Normalization of the equations is especially important in preventing an ill conditioned system. All dependent simulation variables are thus normalized using appropriate scales. Due to the size of the problem, the matrix is inverted using an iterative Krylov subspace method in parallel. The type of Krylov method used in this simulation is the generalized minimum residual (GMRES) along with an additive Schwarz (ASM) preconditioning matrix [28], [29].

C. Boundary Condition Instabilities

A variation of the PML originally proposed by [25] is implemented to absorb outgoing electromagnetic radiation. The PML used in this paper is a frequency-domain adaptation of the convolutional PML (CPML) based on [30]. Because virtually all PML derivations begin with a frequency-domain representation, the implementation into our model is straightforward.

Regardless of the PML type used, all PML derivations follow the same basic principle. This principle is to match the tangential component of the wave numbers at the computational/PML interface. This matching is continued throughout the layers of the PML. Attenuation is realized with the addition of an artificial imaginary component of the wave normal vector \vec{k} . In most applications of computational electromagnetics, the PML accomplishes this task by absorbing the wave function in the direction orthogonal to the PML interface [25].

Two recent papers that discuss issues with the PML related to our study are [26] and [31]. The work of [26] highlights the fact that for a wave in which the group and phase velocities are

antiparallel at the PML interface, the wave experiences exponential growth inside of the PML. Becache *et al.* [26] demonstrate this problem in orthotropic media, but do not present any recommendations as to the resolution of this dilemma.

Cummer [31] examines the properties of a traditional PML in the presence of negative index of refraction materials (NIM). Within a material that possesses a negative index of refraction, antiparallel group and phase velocities are ubiquitous at a particular frequency within the computational space. This condition exists at all PML interfaces. In the case of [31], a relatively simple fix is incorporated in the model to allow for proper absorption of outgoing waves. Unfortunately, this method does not work in a magnetized plasma, since the switch of [31] is only frequency dependent, while, as shown below, in a cold magnetized plasma, antiparallel group and phase velocity behavior is both direction (i.e., k -vector) and frequency dependent.

Using the stretched coordinate version of the PML, first derived in [32], we now show the manifestation of the PML region instability for a cold magnetized plasma. This instability is not just a cold plasma phenomena, but exists in any electromagnetic plasma model that utilizes a PML as an absorbing boundary condition.

D. PML Derivation

The derivation of the PML is well documented and can be found in numerous papers and books, including [25] and [21]. A brief description of the PML suffices to illustrate the problem at hand. In a conventional stretched coordinate PML, the nabla operator used in Maxwell's equations is replaced by the nabla operator given by

$$\tilde{\nabla} = \hat{x} \frac{1}{s_x} \frac{\partial}{\partial x} + \hat{y} \frac{1}{s_y} \frac{\partial}{\partial y} + \hat{z} \frac{1}{s_z} \frac{\partial}{\partial z} \quad (4)$$

where s_x , s_y , and s_z denote stretching variables in their respective coordinate directions [32]. The form of the stretching variable is given by

$$s = \left(1 + \frac{\alpha}{j\omega} \right) \quad (5)$$

where ω represents radian frequency and α describes an attenuation constant that exists only within the PML. Denoting the region inside the computational domain as *region 1* and the interior of the PML as *region 2*, and assuming planewave solutions, the relationship between the wave numbers inside and outside the PML are given by

$$k_2 = \left(1 + \frac{\alpha}{j\omega} \right) k_1. \quad (6)$$

For simplicity, we assume a uniform planewave in 1-D propagating in the $+\hat{x}$ direction. The wave number k_2 admits planewave solutions inside of the PML given by

$$e^{-jk_{x1}(1+(\alpha/j\omega))x} \quad (7a)$$

or

$$e^{-jk_{x1}x} e^{(-\alpha k_{x1}/\omega)x}. \quad (7b)$$

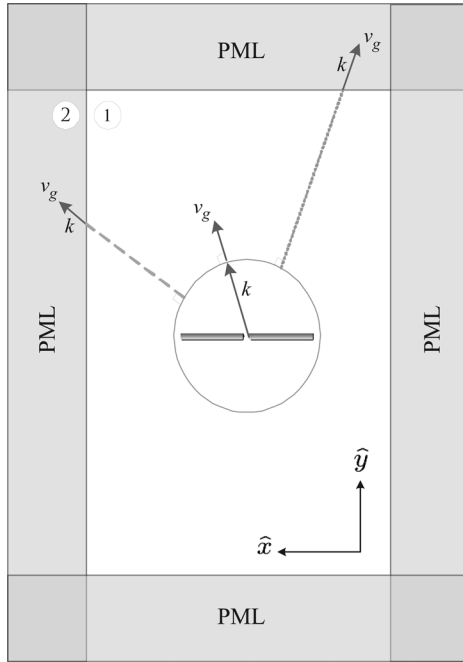


Fig. 4. Free-space isotropic refractive index surface.

Becache *et al.* [26] state that an instability develops if, for a given mode, the perpendicular components of the \vec{k} -vector and group velocity vector \vec{v}_g are antiparallel at the entrance of the PML. This result can be ascertained by examination of the exponential attenuation term in (7b). If a wave possesses a component of group velocity \vec{v}_g in the $+\hat{x}$ direction and component of \vec{k} in the $-\hat{x}$ direction, the fields exponentially grow inside the PML as opposed to the exponential decay as desired.

To illustrate this concept, we make use of the refractive index surfaces for propagation in both free space and a cold magnetized plasma and discuss the differences in the context of the PML. The refractive index surface describes the relative directions of \vec{v}_g and \vec{k} .

E. PML in Free Space

In free space, the refractive index surface is a sphere of unit radius and its cross section is shown as the circle surrounding the antenna in Fig. 4. The \vec{k} in the interior of the sphere represents the initial wave launched from the antenna and the group velocity direction is normal to the refractive index surface. It is readily seen from the free-space refractive index surface of Fig. 4 that all components of the group velocity and k -vector are parallel within the medium and at the PML interface. According to [26] and (7b), this constitutes a stable system, with the wave attenuating inside the PML. However, in a magnetized plasma, the refractive index surface is highly anisotropic and thus dependent on the k -vector direction.

F. PML in the Whistler Mode

For the purpose of the present development, we are interested in waves with frequencies below the electron gyrofrequency, also known as whistler-mode waves. Characteristics of this propagation mode are illustrated by the dispersion diagrams

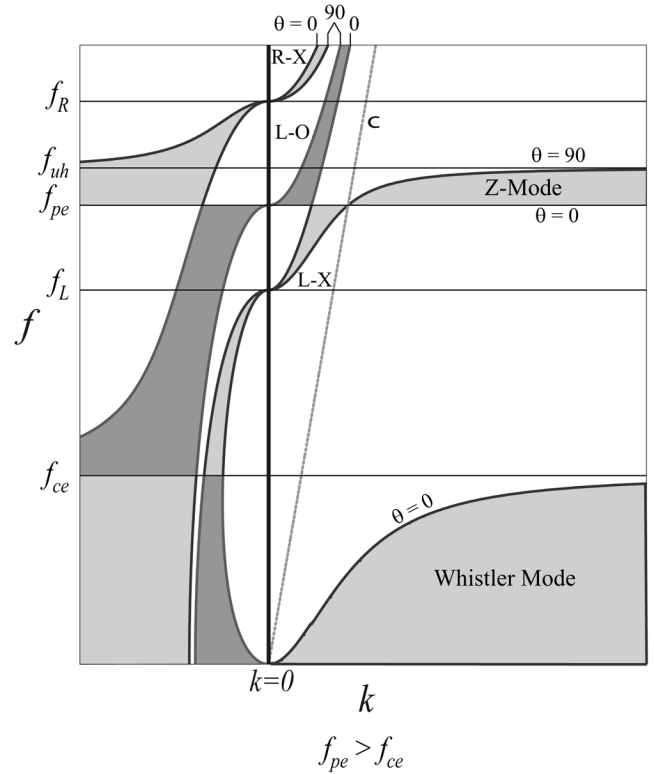


Fig. 5. Cold plasma dispersion diagram where θ represents the propagation direction with respect to the background magnetic field. $k > 0$ corresponds to the real part of the wave number. $k < 0$ corresponds to the imaginary part of the wave number. $R \equiv$ right-handed mode. $L \equiv$ left-handed mode. $O \equiv$ ordinary mode. $X \equiv$ extraordinary mode. $f_R \equiv$ Right-hand cutoff frequency. $f_L \equiv$ left-hand cutoff frequency. $f_{uh} \equiv$ upper hybrid frequency. $f_{pe} \equiv$ plasma frequency. $f_{ce} \equiv$ electron gyrofrequency.

of Figs. 5 and 6 adapted from [33, pp. 356–392] where Fig. 6 represents an expanded region around f_{LHR} .

The LHR frequency in Fig. 6 is a branch that exists when ions are included in the cold plasma formulation. For the case when the ratio of electron plasma frequency to electron gyrofrequency is high, its value is approximately equal to [34, pp. 30–32]

$$f_{LHR} \simeq \sqrt{f_{ce} f_{ci}} \quad (8)$$

where f_{ce} and f_{ci} are the electron and ion gyrofrequencies, respectively. It is important to note that all wave numbers less than zero in Fig. 5 represent imaginary wave numbers corresponding to evanescent modes, while those greater than zero represent propagating modes. Though we are mainly interested in whistler-mode propagation, the dispersion diagram of Fig. 5 contains frequencies in the HF range including the Z-mode branch [2] for completeness. Waves propagating in the Z-mode exhibit simultaneous electrostatic and electromagnetic behavior and, as shown in Section III-H, PML instabilities exist in this frequency range as well.

For frequencies between f_{LHR} and f_{ce} , wave propagation in directions orthogonal to the static magnetic field is not possible and such wave energy is thus strictly evanescent. For $f_{LHR} < f < f_{ce}$, the resonance cone angle is defined as the angle between the direction orthogonal to the background magnetic field

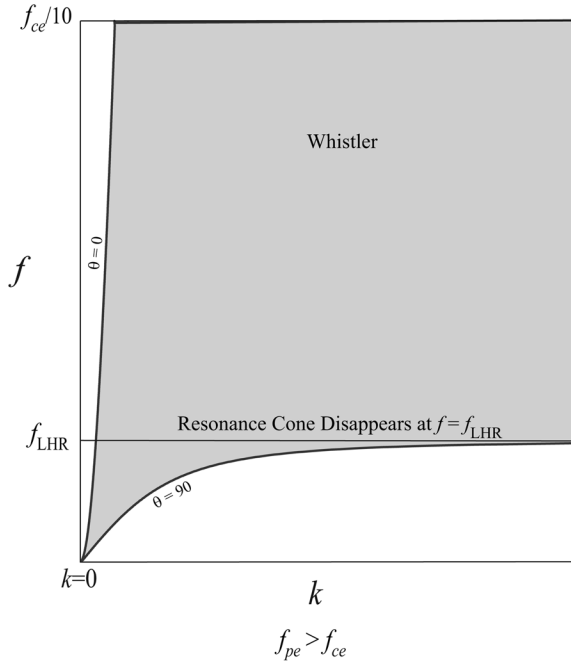


Fig. 6. Dispersion diagram of whistler-mode including LHR frequency.

and the cone along which the refractive index tends to infinity as shown in Fig. 7. Example refractive index surfaces for frequencies above and below the local LHR frequency are shown in Figs. 7 and 8, where \vec{k} represents the wave number, \vec{v}_g is the group velocity or velocity of energy flow given by the normal to the refractive index surface, and θ_{res} is the resonance cone angle discussed earlier. The refractive index surfaces depicted in Figs. 7 and 8 are functions of the wave normal angle, defined as the angle between \vec{k} and the ambient magnetic field. The Gendrin angle is the nonzero wave normal angle at which the group velocity is parallel with the static magnetic field [35]. The Gendrin angle θ_g is illustrated in Fig. 7 and for high ratios of (f_{pe}/f_{ce}) is given approximately by the relation [35]

$$\cos \theta_g \approx \frac{2\omega}{\omega_{ce}} \quad (9)$$

where ω and ω_{ce} are the angular wave frequency and electron gyrofrequencies, respectively. For angles $\theta < \theta_g$, all components of \vec{v}_g and \vec{k} are in the same relative direction. However, for wave normal angles beyond the Gendrin angle, i.e., $\theta > \theta_g$, the components of \vec{v}_g and \vec{k} , which are orthogonal to the static magnetic field, are antiparallel when entering the PML as shown in Fig. 9. Whistler-mode waves with a wave normal angle greater than the Gendrin angle, such as the wave denoted by “1” in Fig. 9, exhibit exponential growth in the PML per (7b). This growth occurs because the PML shown to be unstable in Fig. 9 is designed to absorb waves with wave normals in the $+\hat{x}$ direction or waves of the form e^{-jk_1x} . Because the \hat{x} component of \vec{k} is negative at the PML interface (and thus immediately inside it), the wave fields experience nonphysical growth inside the PML. Wave “2” is attenuated in the PML because the \hat{y} components of \vec{k} and \vec{v}_g are parallel at the PML interface.

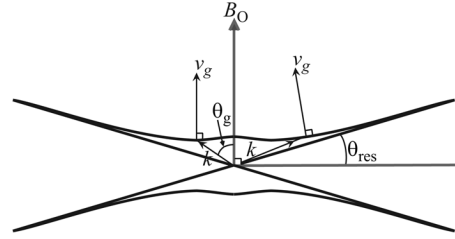


Fig. 7. Refractive index surface for $f_{LHR} < f < f_{ce}/2$.

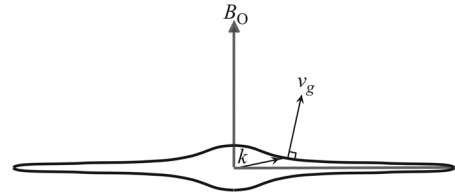


Fig. 8. Refractive index surface for $f_{ci} \ll f < f_{LHR}$.

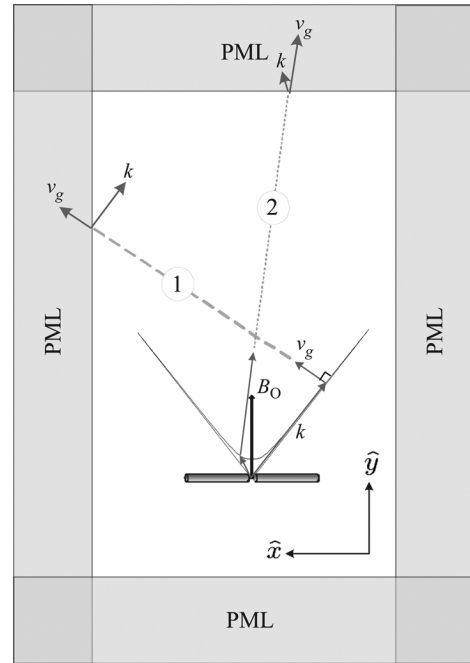


Fig. 9. Unstable PML for whistler-mode propagation.

G. Solution to PML Instability in Whistler Mode

The NIMs discussed by [31] present a similar problem with antiparallel group and phase velocities. In the NIMs of [31], the antiparallel group and phase velocity condition occurs at a particular frequency and is independent of the direction of \vec{k} . Furthermore, in the case of the NIMs, the group and phase velocity vectors are exactly antiparallel, i.e., are at 180° with respect to one another. A simple frequency-dependent adjustment to the stretching parameter of (5) is all that is needed to compensate for the PML instability. In a magnetized plasma, the situation is more complex with the group velocity and k -vectors being both frequency and direction dependent, and being at a varying

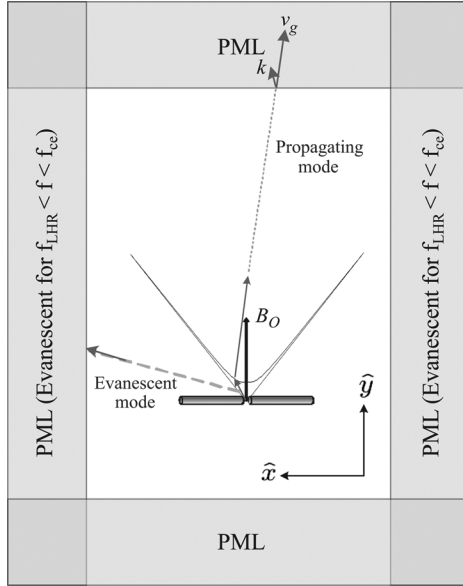


Fig. 10. Evanescent boundary conditions for PML in whistler mode.

angle (that is neither zero nor 180°) with respect to one another. Thus, the stretching parameter, in addition, must incorporate information about \vec{k} . We have chosen to incorporate a specially adapted form of the PML that has been tailored to isolate and absorb evanescent modes in the directions orthogonal to the static magnetic field as shown in Fig. 10 for frequencies $f, f_{LHR} < f < f_{ce}$. For frequencies $f, f_{ci} \ll f < f_{LHR}$, however, the aforementioned instability is not present. Though the refractive index surface of Fig. 8 is highly anisotropic at these frequencies, for the PML surface alignment shown in Fig. 9, there is no k -vector for which the directional components of \vec{k} and \vec{v}_g are antiparallel, and thus, a PML can be made to absorb both propagating and evanescent modes in this frequency range.

Numerical errors due to the reflection of propagating modes from the evanescent boundary conditions do not pose an issue for antennas oriented perpendicular to the static magnetic field at whistler-mode frequencies. For frequencies well below the electron gyrofrequency, the refractive index surface is virtually flat with the resonance cone angle being within a few degrees of the direction orthogonal to the static magnetic field. In this case, most of the wave energy is focused into the PML parallel to the static magnetic field and the evanescent modes are absorbed by the PML in the direction orthogonal to the static magnetic field.

A strictly evanescent PML can be realized by utilizing the formulation given in [30]. For simplicity, we only show the \hat{x} component. From [30, eq. (7)], we have

$$\nabla_{x\text{PML}} = \left[1 - b_{x0} - \left(\sum_{n=1}^N \frac{b_{xn}\alpha_{xn}}{j\omega + \alpha_{xn}} \right) \right] \frac{\partial}{\partial x} \hat{a}_x \quad (10)$$

where $\nabla_{x\text{PML}}$ is the modified ∇ operator inside the PML, b_{x0} is a factor that controls evanescent attenuation for nonpropagating modes, and $(b_{xn}\alpha_{xn}/(j\omega + \alpha_{xn}))$ are terms that control the attenuation of simultaneous propagating and evanescent modes. Because the inclusion of any terms in the $(b_{xn}\alpha_{xn}/(j\omega + \alpha_{xn}))$ sequence produces amplification inside of the PML orthogonal

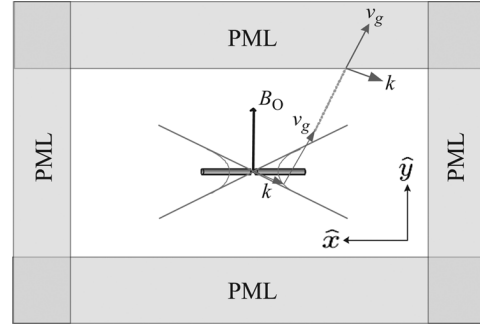


Fig. 11. Unstable PML for Z-mode propagation.

to the static magnetic field, these terms are removed. Thus, a strictly evanescent PML for the \hat{x} direction is given by

$$\nabla_{x\text{PML}} = [1 - b_{x0}] \frac{\partial}{\partial x} \hat{a}_x \quad (11)$$

where b_{x0} represents a conductivity profile that varies from 0 at the PML interface to 1 at the last PML layer in a low-order polynomial fashion.

H. Z-Mode Instability

Analogous to the PML that amplifies waves in the whistler mode, Z-mode wave propagation [34] for frequencies between the plasma frequency and upper hybrid frequency as shown in Fig. 5 exhibits these same instabilities within the PML. Fig. 11 illustrates this instability in conjunction with the Z-mode refractive index surface.

It is seen from Fig. 11 that the PML oriented perpendicular to the magnetic field that attenuates waves at frequencies in the whistler mode is now unstable for Z-mode propagation. An important benefit of the FDFD method is that it allows us to isolate a particular frequency of interest without exciting transients at other frequencies due to broadband numerical noise. These transients are fundamental characteristics of time-domain simulations methods such as FDTD. Because we are not concerned with propagation at these higher frequencies for the purpose of radiation belt electron precipitation by VLF waves, this HF branch can be ignored. However, for time-domain simulations, this issue would need to be specifically addressed.

I. Computational Mesh Considerations

The computational grid used in our model is a nonuniform Cartesian mesh. For propagation at wave normal angles close to the resonance cone, the theoretical wavelength drops to zero in the cold plasma limit, and is thus not properly resolved on a mesh with finite cell size. As a consequence, waves propagating with wave normal angles close to the resonance cone realize wavelengths on the order of the mesh cell size regardless of the cell resolution.

With the inclusion of an antenna, however, it has been verified in our simulation that if the antenna is well resolved by the largest cell size used in the computational space (i.e., 30 cells over the length of the antenna), it is not necessary to realize zero wavelengths using finite size cells. Thus, increasing the cell resolution beyond 30 cells does not adversely affect the

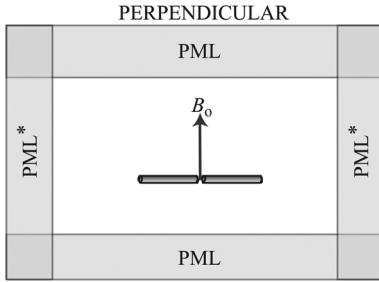


Fig. 12. Computational domain for cold plasma simulations. The PML boundary conditions orthogonal to the magnetic field and denoted by PML* are evanescent for $f_{LHR} < f < f_{ce}$.

impedance values since the waves dominating the energy flow are well resolved. This observation is supported by [12] and [13] where it was found that dipole antennas operating in a magnetized plasma environment preferentially radiate waves whose wavelength is on the order of the antenna length.

IV. SIMULATION RESULTS

We now present results for the current distributions and input impedance of electric dipole antennas in a magnetized plasma. FDFD simulations are carried out for dipole antennas oriented perpendicular with respect to the ambient static magnetic field. This orientation is chosen since the antenna pattern and power delivery are optimal for launching waves parallel to the static magnetic field [12], [13]. Antennas considered for the purpose of our application are on the order of 100 m in length and up to 20 cm in diameter. The orientations of these antennas with respect to the static magnetic field are shown in Fig. 12.

The FDFD method is well suited to model small geometries with respect to a free-space wavelength. The antenna itself is assumed to be a perfect electric conductor (PEC) and the current distribution along the length of the antenna is calculated by taking a line integral of the frequency-domain magnetic field components encircling each wire element along the length of the antenna. The input impedance is calculated using

$$Z_{in} = \frac{V(f)}{I(f)} = \frac{(\int \vec{E} \cdot d\vec{l})_{feed}}{(\oint \vec{H} \cdot d\vec{l})_{feed}} \quad (12)$$

where the field quantities are already in the frequency domain per use of the FDFD method. Equation (12) represents the ratio of the complex phasors quantities for the current and voltage at the terminals of the antenna.

For the purposes of our simulation, we first examine the properties of a 100-m-long electric dipole antenna in a cold magnetized plasma operating near $L = 2$ in the magnetic equatorial plane. We consider an electron-proton plasma with $f_{pe} = 401$ kHz and $f_{ce} = 110$ kHz in a collisionless environment. The computational meshes for a 100-m antenna are shown in Fig. 13 representing the geometries for frequencies above and below f_{LHR} . The \hat{z} directed antenna is located in the center of the space and is 20 cm in diameter, which corresponds to the smallest cell size in the space. The magnetic field is oriented in the $+\hat{y}$ direction and a PML is used to truncate the space in all directions. The dipole antenna is excited with an \vec{E}_z hard source in the gap between the conducting elements with a value

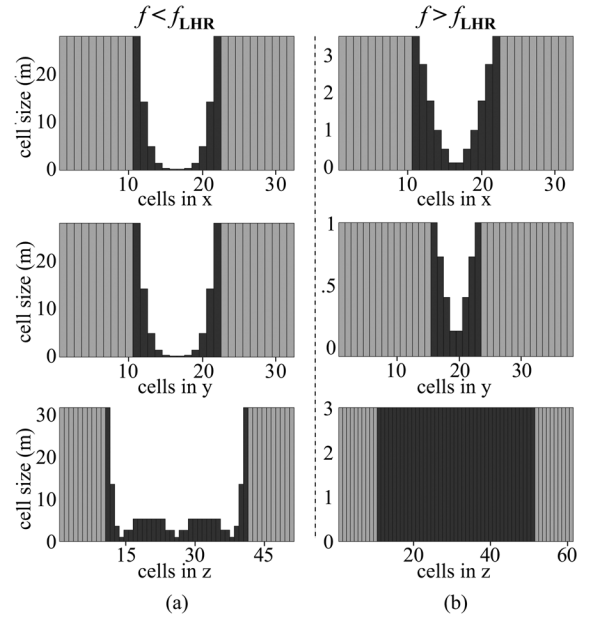


Fig. 13. Variation in cell size along each of the principal directions for nonuniform mesh used in simulation at $L = 2$. The dark gray cells correspond to those that are within the computational domain and the light gray cells correspond to the PML layers. (a) Frequencies below f_{LHR} with $(\hat{x}, \hat{y}, \hat{z})$ dimensions $32 \times 32 \times 51$. (b) Frequencies above f_{LHR} with $(\hat{x}, \hat{y}, \hat{z})$ dimensions $32 \times 38 \times 61$.

of 1 V/m and the system is allowed to converge with a relative residual norm of 10^{-6} .

One of the primary benefits of using frequency over time-domain analysis is the ability to use a different mesh and PML configuration for each simulation run. Though we do not use this advantage to the full extent available (a different configuration for each frequency), we do use a different mesh and PML configuration for frequencies below and above f_{LHR} for which the propagation characteristics are quite different as previously shown in Figs. 7 and 8. For frequencies $f > f_{LHR}$, there exists a range of k -vectors for which the refractive index is very large and tending to infinity at the resonance cone angle θ_{res} as shown in Fig. 7. It is, therefore, imperative to utilize much smaller cells to capture these tiny wavelengths resulting from the high refractive index relative to those used for frequencies $f < f_{LHR}$ as shown in Fig. 13. For frequencies below f_{LHR} , the resonance cone disappears as shown in Fig. 8 with the refractive index surface being closed and possessing a maximum of $n \approx 600$ at directions orthogonal to the background magnetic field. The refractive index surface for $f < f_{LHR}$ becomes more isotropic with decreasing frequency and thus larger cell sizes may be used as shown in Fig. 13(a). It is this difference in refractive index between the two frequency regimes that explains why the cell size along the \hat{z} direction corresponding to the length of the antenna stays at a constant 3 m for $f > f_{LHR}$ while the cell size is variable for $f < f_{LHR}$.

As with the computational mesh, the PML configuration is different for frequencies above and below f_{LHR} . For frequencies $f > f_{LHR}$, the PML consists of ten cells in the \hat{x} direction, 15 cells in the \hat{y} direction, and ten cells in the \hat{z} direction. The

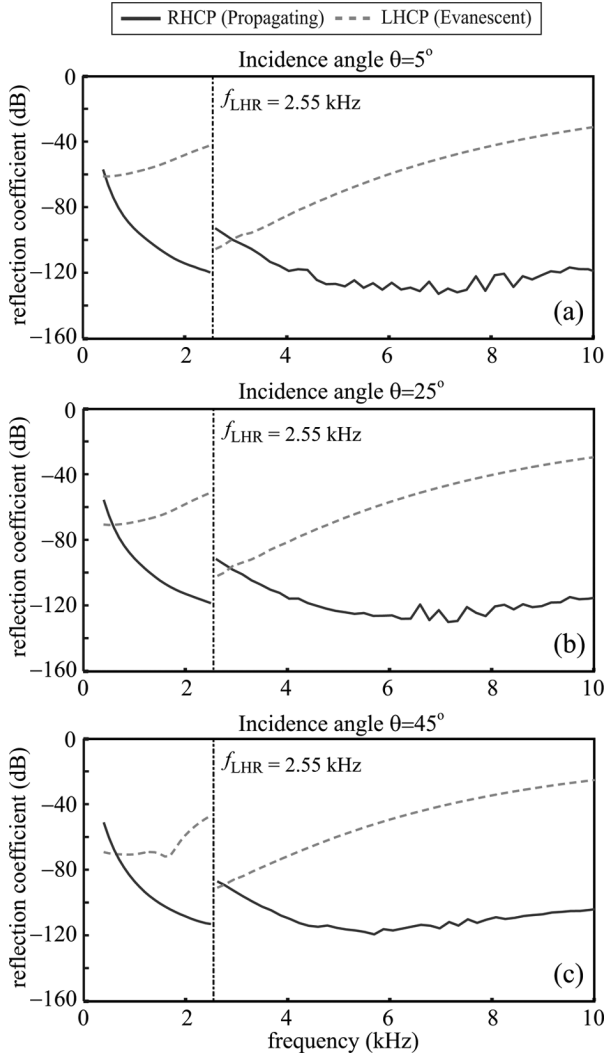


Fig. 14. Reflection coefficient calculations for PML oriented along \hat{y} direction, parallel to the static magnetic field, for angles of 5° , 25° , and 45° with respect to normal incidence. RHCP and LHCP incident wave polarizations are shown including the performance for frequencies above and below f_{LHR} .

PML layers in both the \hat{x} and \hat{z} directions are made to absorb only evanescent waves, while the PML layers in the \hat{y} direction absorb both propagating and evanescent waves in this frequency range. These layers, along with the computational mesh, are illustrated in Fig. 13. For frequencies below f_{LHR} , there are ten PML layers in all directions and each PML is made to absorb both propagating and evanescent waves. The PML parameters are different for frequencies above and below f_{LHR} because the cell sizes and refractive index surfaces are quite different in the two cases. The PML performance up to 10 kHz including frequencies above and below f_{LHR} for the simulations in the $L = 2$ environment are shown in Figs. 14 and 15 corresponding to PML orientations parallel and perpendicular to the static magnetic field, respectively.

There are several things to notice about the plots of Figs. 14 and 15. First, the only propagating modes in the frequency range $f_{ci} \ll f < f_{ce}$ where $f_{ci} \ll f_{LHR}$ are right-hand circularly

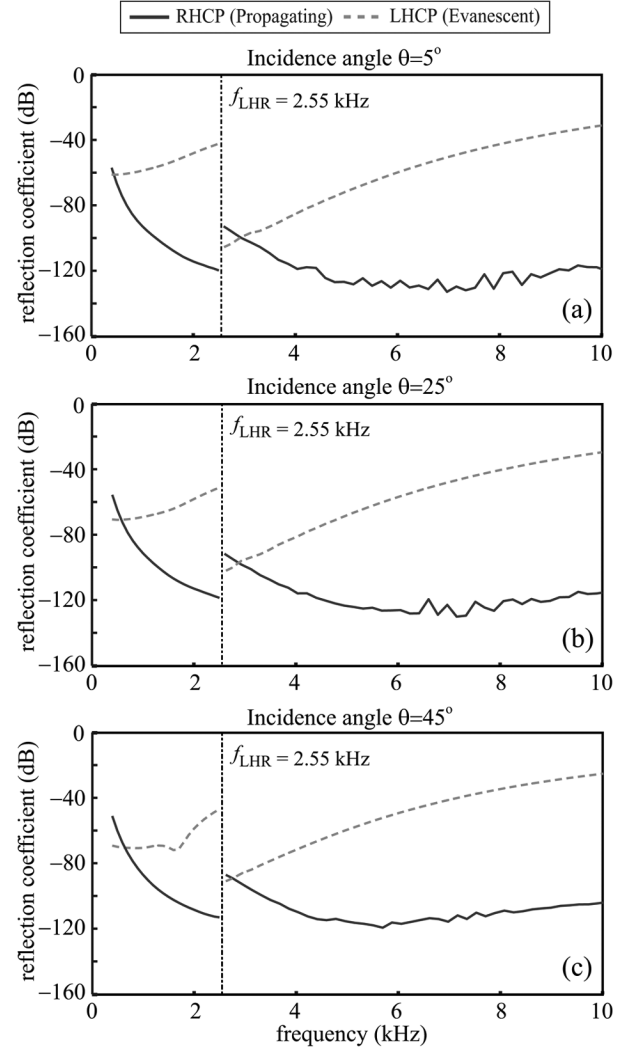


Fig. 15. Reflection coefficient calculations for PML oriented in \hat{x} and \hat{z} directions, perpendicular to the static magnetic field, for angles of 5° , 25° , and 45° with respect to normal incidence. RHCP and LHCP incident wave polarizations are shown including the performance for frequencies above and below f_{LHR} .

polarized (RHCP). All waves launched from the antenna that are left-hand circularly polarized (LHCP) are evanescent in the plasma at these frequencies. The discontinuity in the reflection coefficient calculations at f_{LHR} is a direct result of the differences in mesh and PML geometries across this transition region as stated earlier. Though the PML performance for LHCP waves representing the directions orthogonal to the static magnetic field described by Fig. 15 is relatively poor, these waves will reflect into the PML parallel to the static magnetic field of Fig. 14 and be absorbed with greater attenuation. As mentioned in Section III-G, the PML in the direction orthogonal to the static magnetic field as represented in Fig. 15 for frequencies $f > f_{LHR}$ has been tailored to absorb evanescent waves only to avoid the PML instabilities mentioned earlier. As a result, the incident RHCP propagating modes experience no attenuation and are perfectly reflected. Finally, there is a small section in Fig. 15(a) in the range $9.2 < f < 10$ kHz for which the incident RHCP wave is evanescent. The resonance cone angle of

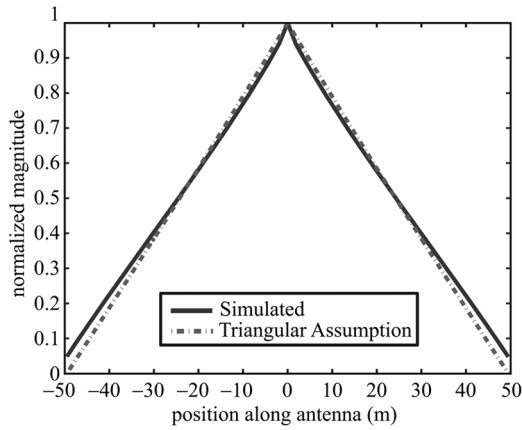


Fig. 16. $L = 2$ current distribution for a 100-m antenna at $f = 400$ Hz driving frequency.

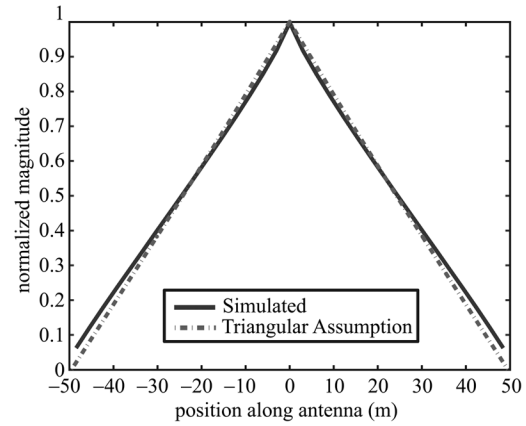


Fig. 19. $L = 2$ current distribution for a 100-m antenna at $f = 10.0$ kHz.

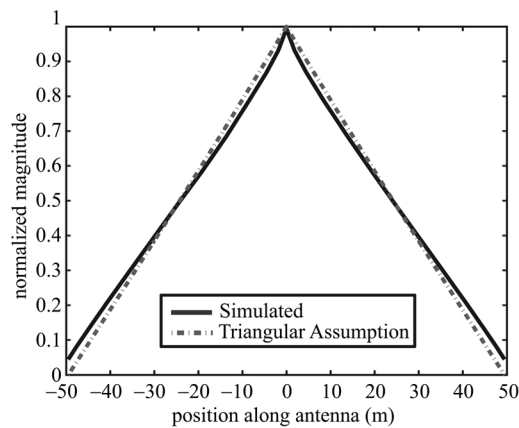


Fig. 17. $L = 2$ current distribution for a 100-m antenna at $f = 2.0$ kHz driving frequency.

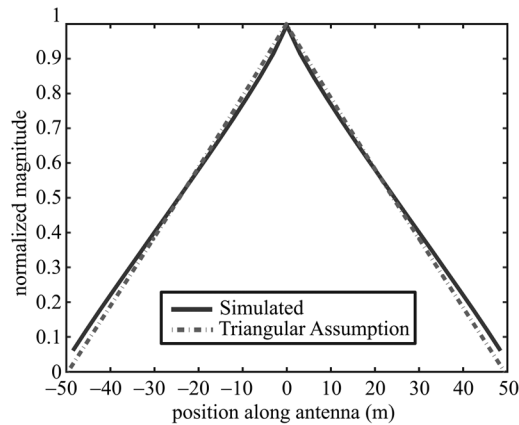


Fig. 18. $L = 2$ current distribution for a 100-m antenna at $f = 2.6$ kHz.

Fig. 7 is 5° at ≈ 9.2 kHz and marks the point at which the incident RHCP waves become evanescent and able to be absorbed by this PML.

A. Current Distributions and Input Impedance Calculations for a 100-m Antenna at $L = 2$

The first case study is a 100-m antenna located in the equatorial plane at $L = 2$. We compare the current distributions for

frequencies above and below the local LHR frequency which is $f_{\text{LHR}} = 2.55$ kHz. Figs. 16 and 17 represent the current distributions for two frequencies below f_{LHR} . It can be seen from Figs. 16 and 17 that the current distributions are virtually identical to the assumed triangular distribution of [9]–[11]. One important point is that for a simulated antenna of finite thickness, the current is nonzero at the ends, contrary to the ideal case, since the finite area allows for a buildup of charge at the tips. The simulation results thus reflect this realistic condition much better than the idealized case shown in dashed lines. Figs. 18 and 19 represent the current distributions for two frequencies above f_{LHR} . Once again, there is no significant deviation from the assumed triangular distribution, except for the realistic end-effect due to the finite antenna radius.

Fig. 20(a) and (b) compares the simulated input impedance of the 100-m dipole antenna at $L = 2$ with results obtained from [9]–[11]. Fig. 20(b) represents an expanded portion of Fig. 20(a) showing the zero impedance point in finer detail. The plots for both the resistance and the reactance calculated with our numerical simulation are in good agreement with those evaluated analytically by [9]–[11]. Below f_{LHR} , [9]–[11], predict the reactance to vary from approximately 100Ω at zero frequency to ∞ at the LHR frequency. Unlike with the quasi-electrostatic assumption of [6], the works of [9]–[11] predict the resistance to have a nonzero value below the LHR frequency ranging from 0Ω at zero frequency to ∞ at the LHR frequency. These trends are reflected in the simulated results as shown in Fig. 20(a) and (b). Above f_{LHR} , the analytical reactance varies from 0Ω to about -8Ω at 10 kHz. The simulated results in these regimes are within about 15Ω .

The disparity between the analytical and simulated results in Fig. 20(b) is attributed to a combination of theory and numerical accuracy of the FDFD technique. The authors of [9]–[11] assume a triangular current distribution with zero current at the tips of the antenna. In reality, an antenna possessing finite width will support current at the tips of the antenna as shown in the simulation plots of Figs. 16–19. Additionally, the use of cells which are at least 10^4 times smaller than the corresponding free-space wavelength results in convergence issues for the associated FDFD matrix. The large ratio of wavelength to cell size produces a matrix with vastly different eigenvalues and

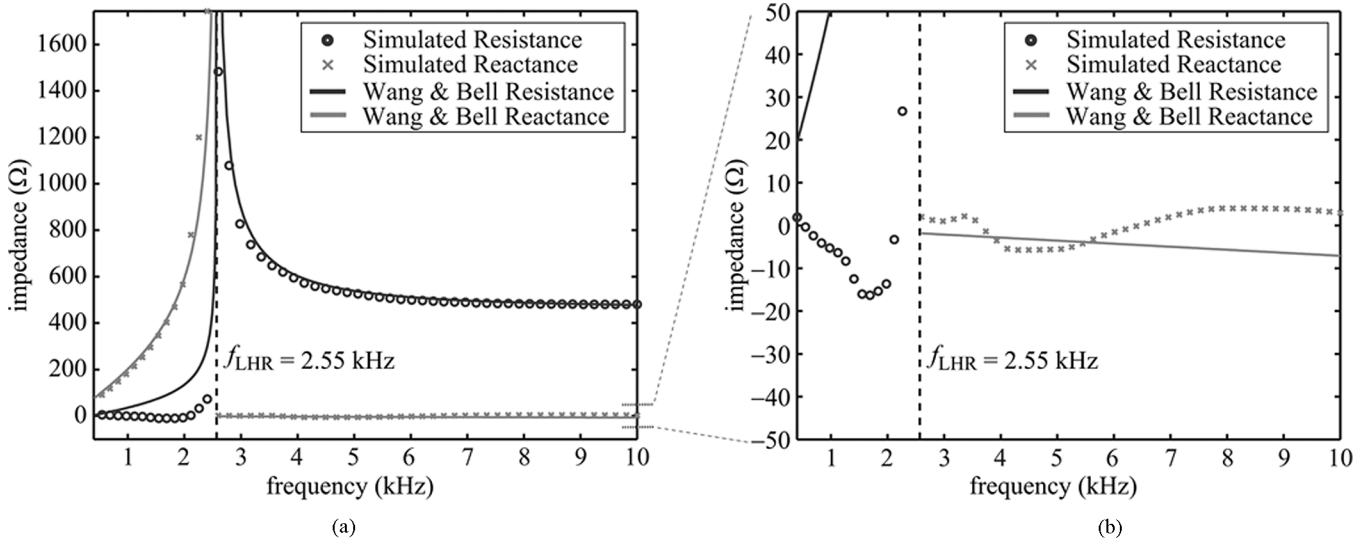


Fig. 20. Input impedance for a 100-m antenna at $L = 2$. (a) Full range response. (b) Expanded region around zero impedance.

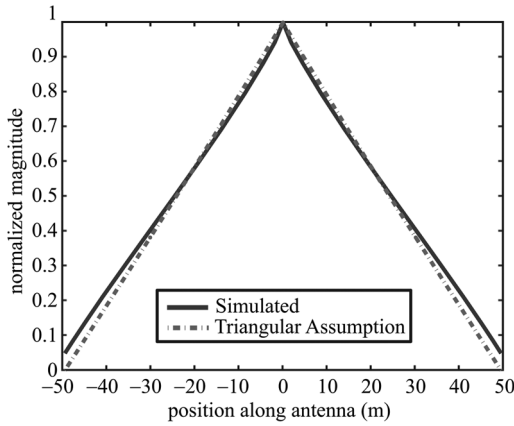


Fig. 21. $L = 3$ current distribution for a 100-m antenna at $f = 460$ Hz driving frequency.

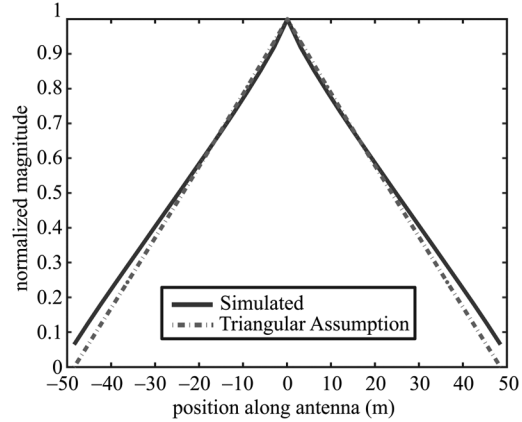


Fig. 22. $L = 3$ current distribution for a 100-m antenna at $f = 4.0$ kHz driving frequency.

thus a large condition number; a limitation of the frequency-domain method in this regime. This limitation is readily seen in Fig. 20(b) for which there exist impedance values that possess a negative resistance below the LHR frequency.

B. Current Distributions and Input Impedance Calculations for a 100-m Antenna at $L = 3$

The second case study examines the properties of a 100-m antenna located at $L = 3$ in the equatorial plane. Typical values of the plasma and gyrofrequencies at $L = 3$ are $f_{pe} = 284$ kHz and $f_{ce} = 32.6$ kHz, respectively. Because the computational mesh geometry of Fig. 13 and the PML performance characteristics of Figs. 14 and 15 are very similar to the simulation setup at $L = 2$, these characteristics are not shown. Only two different examples of the current distribution are given since they are not markedly different than those for the cases of an antenna at $L = 2$. Figs. 21 and 22 represent the current distributions for frequencies above and below $f_{LHR} = 761$ Hz. It can be seen from Figs. 21 and 22 that there is no significant deviation from

a triangular current distribution for an antenna subject to a decrease in plasma and gyrofrequencies. Fig. 23(a) and (b) compares the simulated input impedance of the 100-m dipole antenna at $L = 3$ with results obtained from [9]–[11]. As with the results from the previous case study, the impedance characteristics in Fig. 23 exhibit very good agreement with the work of [9]–[11].

V. NONTRIANGULAR CURRENT DISTRIBUTIONS

For the 100-m antennas we have considered thus far operating at both $L = 2$ and $L = 3$ in the equatorial plane, the current distributions have remained virtually triangular. We now show that there exist cases for which these electrically short antennas operating at VLF frequencies exhibit current distributions that decay exponentially along the length of the antenna as a result of their orientation lying within the evanescent region of the refractive index surface for frequencies above f_{LHR} . For this purpose, we consider antennas operating at $L = 2$ only and consider variations in length and plasma frequency while keeping the gyrofrequencies constant. For these comparisons, f_{LHR} is unchanged and has a value of 2.55 kHz.

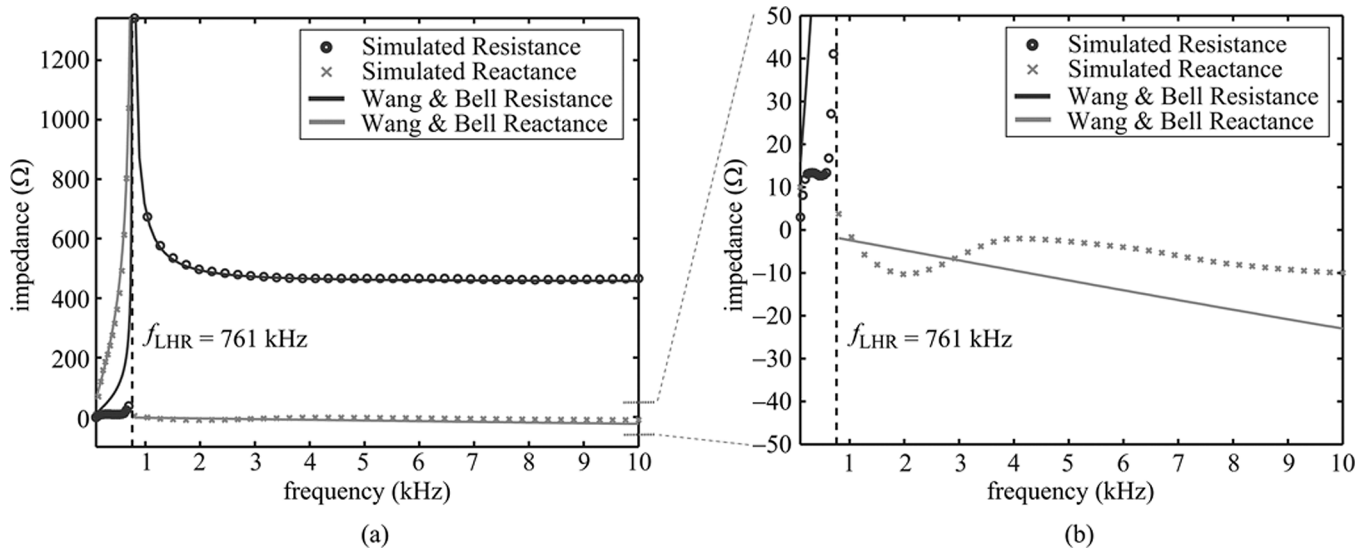


Fig. 23. Input impedance for a 100-m antenna at $L = 3$. (a) Full range response. (b) Expanded region around zero impedance.

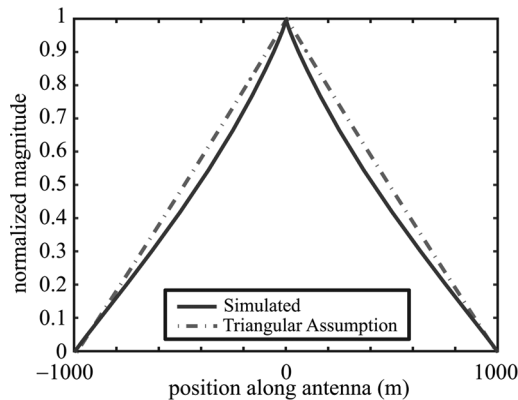


Fig. 24. Current distributions for 2000-m-long antenna at $L = 2$ operating at 5 kHz.

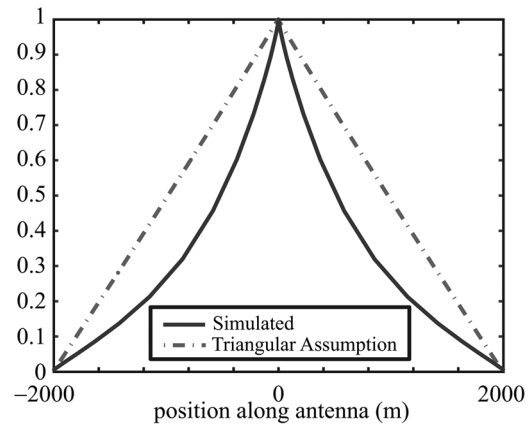


Fig. 25. Current distributions for 4000-m-long antenna at $L = 2$ operating at 5 kHz.

A. Long Antennas

First, we consider the effects of an increase in antenna length, keeping all plasma parameters constant, corresponding to conditions found at $L = 2$. Figs. 24 and 25 show the current distribution for linear antennas that are 2000 and 4000 m corresponding to lengths which are factors of 30 and 15 smaller than the equivalent free-space wavelength, respectively.

It is seen from Fig. 24 that for a 2000-m antenna, the current distribution only slightly deviates from the triangular assumption whereas for the 4000-m antenna shown in Fig. 25 the current experiences substantial decay, which would result in a significant decrease in the dipole moment, thereby reducing the radiation resistance. Thus, dipole antennas that exhibit this type of exponential decay along the length of the elements would not be as efficient at delivering power to the medium, and therefore, are not as useful as wave-injection instruments.

B. High Plasma Frequency

An increase in the local plasma frequency, keeping all other factors unchanged, results in a similar exponential decrease in the antenna current distribution. In this case, we examine a

100-m-long antenna operating at an augmented $L = 2$ plasma environment by adjusting only the local plasma frequency f_{pe} to values of 10 and 20 MHz. These results are shown in Figs. 26 and 27.

Figs. 26 and 27 correspond to plasma frequencies that are roughly 20 and 40 times the normal value at $L = 2$. It is not until the plasma frequency reaches 20 MHz as shown in Fig. 27 that we see a detrimental effect on the current moment as in Fig. 25. Since plasma frequencies that are this high are not typically seen in space environments which are considered in this paper, the example of Fig. 25 is of little concern for a 100-m antenna. However, for future space missions that propose long antenna designs, this adverse effect on the current distribution due to long antenna lengths is an issue that would need to be addressed because there apparently is nothing to be gained by using longer dipole antennas, at least in terms of radiation efficiency.

With respect to the case of high plasma frequency, our simulations have only explored 100-m antennas. However, it is entirely possible that slightly longer antennas orbiting at low altitudes such as in the polar regions of the Earth, where the electron

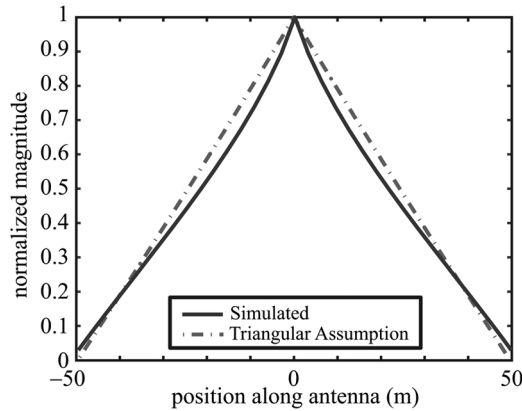


Fig. 26. Current distribution for 100-m antenna operating in plasma with $f_{pe} = 10$ MHz and driving frequency of 5 kHz.

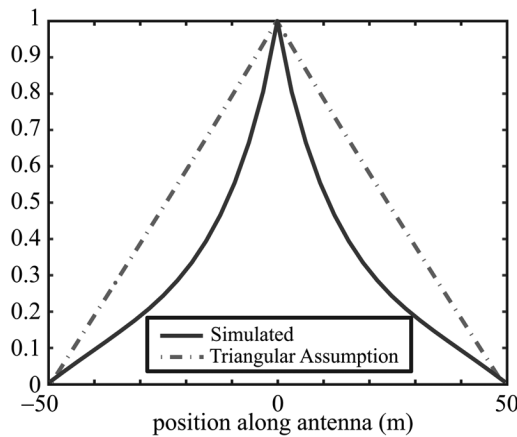


Fig. 27. Current distribution for 100-m antenna operating in plasma with $f_{pe} = 20$ MHz and driving frequency of 5 kHz.

densities can be much larger, would exhibit the same exponential decay as in the previous case study concerning the 4000-m antenna operating in the equatorial region of $L = 2$. Future simulation work using our code could determine this minimum length requirement for a given plasma environment.

VI. CONCLUSION

We have illustrated some of the difficulties in modeling electromagnetic wave propagation in a magnetized plasma and have verified an important assumption inherent in past analytical work, namely, the assumed current distribution along the dipole antenna. The current distribution appears to be triangular for most cases shown at whistler-mode frequencies and our results for the terminal impedance of the dipole antennas studied here agree well with those of analytical work. In addition, we have shown that the current distribution exhibits exponential decay for longer antennas and for environments with large plasma frequencies relative to the conditions listed in our initial case studies. It should be noted that this decay is present even though these same antennas would be considered electrically short in a free-space environment. The 100-m antennas located at both $L = 2$ and $L = 3$ seem to be self-tuning for the frequencies simulated above f_{LHR} in that the reactance curves shown in Figs. 20 and 23 are virtually zero across the range given. With

the current distribution thus verified to be triangular, the results of [12] can be used to determine the power radiation pattern.

This work represents an initial step in the development of a more complete (in terms of the underlying physics) electromagnetic code to self-consistently solve for both the near and far fields generated by electric dipole antennas. The numerical methods including the PML boundary condition utilized herein resolves a number of difficult challenges that are not specific to a cold plasma environment. As such, this work also represents an advance in the numerical study of electromagnetic wave propagation in a magnetized plasma in particular, or more generally for arbitrary anisotropic media.

REFERENCES

- [1] D. Carpenter and R. Anderson, "An isee/whistler model of equatorial electron density in the magnetosphere," *J. Geophys. Res.*, vol. 97, no. A2, pp. 1097–1108, 1992.
- [2] D. Carpenter, T. Bell, U. Inan, R. Benson, V. Sonwalkar, B. Reinisch, and D. Gallagher, "Z-mode sounding within propagation cavities and other inner magnetospheric regions by the RPI instrument on the image satellite," *J. Geophys. Res.*, vol. 108, no. A12, pp. 1421–1421, 2003.
- [3] T. Bell, U. Inan, M. Platino, J. Pickett, P. Kossey, and E. Kennedy, "CLUSTER observations of lower hybrid waves excited at high altitudes by electromagnetic whistler mode signals from the HAARP facility," *Geophys. Res. Lett.*, vol. 31, no. 6, 2004.
- [4] M. Platino, U. Inan, T. Bell, D. Gurnett, J. Pickett, P. Canu, and P. Decreau, "Whistlers observed by the cluster spacecraft outside the plasmasphere," *J. Geophys. Res.*, vol. 110, no. A3, 2005.
- [5] J. Kraus, *Antennas*, 2nd ed. New York: McGraw Hill, 1988.
- [6] K. Balmain, "The impedance of a short dipole antenna in a magnetoplasma," *IEEE Trans. Antennas Propag.*, vol. AP-12, no. 5, pp. 605–617, Sep. 1964.
- [7] K. Balmain, "Antennas in plasma: characteristics as functions of frequency," *Radio Sci.*, vol. 7, no. 8-9, pp. 771–775, 1972.
- [8] K. Balmain, "Properties of antennas in plasmas," *Annales Des Telecommun.*, vol. 34, no. 3-4, pp. 273–283, 1979.
- [9] T. Wang and T. Bell, "Radiation resistance of a short dipole immersed in a cold magnetoionic medium," *Radio Sci.*, vol. 4, pp. 167–177, Feb. 1969.
- [10] K. Balmain, "On VLF radiation resistance of an electric dipole in a cold magnetoplasma," *Radio Sci.*, vol. 5, no. 3, pp. 605–610, 1970.
- [11] T. N.-C. Wang, "VLF input impedance characteristics of an electric antenna in a magnetoplasma," Ph.D. dissertation, Electr. Eng. Dept., Stanford Univ., Stanford, CA, 1970.
- [12] T. Wang and T. Bell, "VLF/ELF radiation patterns of arbitrarily oriented electric and magnetic dipoles in a cold lossless multicomponent magnetoplasma," *J. Geophys. Res.*, vol. 77, pp. 1174–1189, 1972.
- [13] T. Wang and T. Bell, "Electric dipole radiation at VLF in a uniform warm magneto-plasma," *Revue de Physique Appliquee*, vol. 7, no. 1, pp. 11–20, 1972.
- [14] T. Wang and T. Bell, "VLF/ELF input impedance of an arbitrarily oriented loop antenna in a cold collisionless multicomponent magnetoplasma," *IEEE Trans. Antennas Propag.*, vol. AP-20, no. 3, pp. 394–398, May 1972.
- [15] I. Shkarofsky, "Nonlinear sheath admittance, currents, and charges associated with high peak voltage drive on a VLF/ELF dipole antenna moving in the ionosphere," *Radio Sci.*, vol. 7, no. 4, pp. 503–523, 1972.
- [16] R. Stenzel, "Antenna radiation patterns in the whistler wave regime measured in a large laboratory plasma," *Radio Sci.*, vol. 11, pp. 1045–1056, Dec. 1976.
- [17] P. Nikitin and C. Swenson, "Impedance of a short dipole antenna in a cold plasma," *IEEE Trans. Antennas Propag.*, vol. 49, no. 10, pp. 1377–1381, Oct. 2001.
- [18] J. Ward, C. Swenson, and C. Furse, "The impedance of a short dipole antenna in a magnetized plasma via a finite difference time domain model," *IEEE Trans. Antennas Propag.*, vol. 53, no. 8, pt. 2, pp. 2711–2718, Aug. 2005.
- [19] U. Inan, T. Bell, J. Bortnik, and J. Albert, "Controlled precipitation of radiation belt electrons," *J. Geophys. Res.*, vol. 108, no. A5, pp. 1186–1196, 2003.
- [20] T. Chust and G. Belmont, "Closure of fluid equations in collisionless magnetoplasmas," *Phys. Plasmas*, vol. 13, no. 1, 2006.

- [21] A. Taflov and S. Hagness, *Computational electrodynamics : the finite-difference time-domain method*, 2nd ed. Norwood, MA: Artech House, 2000.
- [22] H. Mosallaei and K. Sarabandi, "Magneto-dielectrics in electromagnetics: concept and applications," *IEEE Trans. Antennas Propag.*, vol. 52, no. 6, pp. 1558–1567, Jun. 2004.
- [23] S. Cummer, "An analysis of new and existing FDTD methods for isotropic cold plasma and a method for improving their accuracy," *IEEE Trans. Antennas Propag.*, vol. 45, no. 3, pp. 392–400, Jun. 1997.
- [24] J. H. Lee and D. Kalluri, "Three-dimensional FDTD simulation of electromagnetic wave transformation in a dynamic inhomogeneous magnetized plasma," *IEEE Trans. Antennas Propag.*, vol. 47, no. 7, pp. 1146–1151, Jul. 1999.
- [25] J.-P. Berenger, "A perfectly matched layer for the absorption of electromagnetic waves," *J. Comput. Phys.*, vol. 114, no. 2, pp. 185–200, Oct. 1994.
- [26] E. Becache, S. Fauqueux, and P. Joly, "Stability of perfectly matched layers, group velocities and anisotropic waves," *J. Comput. Phys.*, vol. 188, no. 2, pp. 399–433, Jul. 2003.
- [27] K. Yee, "Numerical solution of initial boundary value problems involving Maxwell's equations in isotropic media," *IEEE Trans. Antennas Propag.*, vol. AP-14, no. 3, pp. 302–307, May 1966.
- [28] S. Balay, K. Buschelman, W. Gropp, D. Kaushik, M. Knepley, L. McInnes, B. Smith, and H. Zhang, PETSc Web Page, 2001 [Online]. Available: <http://www.mcs.anl.gov/petsc>
- [29] S. Balay, K. Buschelman, V. Eijkhout, W. Gropp, D. Kaushik, M. Knepley, L. McInnes, B. Smith, and H. Zhang, *PETSc Users Manual, anl-95/11—Revision 2.1.5*. Argonne, IL: Argonne National Laboratory, 2004.
- [30] M. Chevalier and U. Inan, "A PML using a convolutional curl operator and a numerical reflection coefficient for general linear media," *IEEE Trans. Antennas Propag.*, vol. 52, no. 7, pp. 1647–1657, Jul. 2004.
- [31] S. Cummer, "Perfectly matched layer behavior in negative refractive index materials," *IEEE Antennas Wireless Propag. Lett.*, vol. 3, pp. 172–175, 2004.
- [32] W. C. Chew and W. Weedon, "A 3D perfectly matched medium from modified Maxwell's equations with stretched coordinates," *Microw. Opt. Technol. Lett.*, vol. 7, no. 13, pp. 599–604, 1994.
- [33] M. Kivelson and C. Russell, *Introduction to Space Physics*. Cambridge, U.K.: Cambridge Univ. Press, 1995.
- [34] T. Stix, *The Theory of Plasma Waves*. New York: McGraw-Hill, 1962.
- [35] R. Gendrin, "Le guidage des whistlers par le champ magnetique," *Planetary Space Sci.*, vol. 5, no. 4, pp. 274–278, Aug. 1961.



Timothy W. Chevalier received the B.S. and M.S. degrees in electrical engineering from the University of New Hampshire, Durham, in 1996 and 1998 respectively, and the Ph.D. degree in electrical engineering from Stanford University, Stanford, CA, in 2008.

Currently, he is a Research Associate in the Space, Telecommunications, and Radioscience (STAR) Laboratory, Department of Electrical Engineering, Stanford University. His research interests include numerical simulation of electromagnetic wave propagation in linear and nonlinear media. His current research activities include large scale simulation of the interaction of antennas with a surrounding magnetoplasma environment and propagation of very low frequency (VLF) electromagnetic propagation within the earth-ionosphere waveguide.



Umran S. Inan (S'76–M'77–SM'99–F'06) received the B.S. and M.S. degrees in electrical engineering from the Middle East Technical University, Ankara, Turkey, in 1972 and 1973, respectively, and the Ph.D. degree in electrical engineering from Stanford University, Stanford, CA, in 1977.

Currently, he is a Professor of Electrical Engineering at Stanford University, where he serves as Director of the Space, Telecommunications, and Radioscience (STAR) Laboratory. He actively conducts research in electromagnetic waves in plasmas, lightning discharges, ionospheric physics, and very low frequency remote sensing. He has served as the Ph.D. dissertation adviser for 22 students.

Dr. Inan is a Member of Tau Beta Pi, Sigma Xi, the American Geophysical Union, and the Electromagnetics Academy. He received the 1998 Stanford University Tau Beta Pi Award for Excellence in Undergraduate Teaching. He serves as the current Chair of the United States National Committee of the International Union of Radio Science (URSI) and the International Chair of Commission H (Waves in Plasmas) of URSI.



Timothy F. Bell received the B.S., M.S., and Ph.D. degrees in physics from Stanford University, Stanford, CA, in 1955, 1957, and 1964, respectively.

Currently, he is a Senior Research Associate in the Space, Telecommunications, and Radioscience (STAR) Laboratory, Department of Electrical Engineering, Stanford University. He is currently involved in the theoretical studies of antenna-plasma and wave-particle interactions in the magnetosphere. He has authored or coauthored over 300 papers in the fields of VLF wave-particle interactions, antennas in plasmas, and wave propagation and scattering in anisotropic media; in addition, he has presented more than 300 papers at scientific conferences.

Dr. Bell is a member of Sigma Xi, the International Union of Radio Science (URSI), the American Geophysical Union (AGU), and the California Scholarship Federation.